Calibration of DART 3D model with UAV and Sentinel-2 for studying the radiative budget of conventional and agro-ecological maize fields

P. Boitard, B. Coudert, N. Lauret, S. Queguiner, C. Marais-Sicre, O. Regaieg, Y. Wang, J.-P. Gastellu-Etchegorry

Remote Sensing Applications: Society and Environment 32 (2023) 101079

Contents lists available at ScienceDirect

Remote Sensing Applications: Society and Environment

journal homepage: www.elsevier.com/locate/rsase

Calibration of DART 3D model with UAV and Sentinel-2 for studying the radiative budget of conventional and agro-ecological maize fields

P. Boitard *, B. Coudert, N. Lauret, S. Queguiner, C. Marais-Sicre, O. Regaieg, Y. Wang, J.-P. Gastellu-Etchegorry

Centre d'Etudes Spatiales de la Biosphère - UT3, CNES, CNRS, IRD, Université de Toulouse, 31401, Toulouse, Cedex 9, France

A B S T R A C T

Quantifying the radiative budget (RB) of maize, the world's predominant cereal, is crucial to managing its growth in a context of global warming. Its microclimate including temperature, water, and energy flux depend on crop management practices. This paper compares the influence of agroecological practices (AE) and conventional agriculture (CA) on the RB of maize using three-dimensional (3D) radiative transfer modelling and remote sensing (RS) observations. We studied two neighbour maize fields in south-west France, respectively with AE and CA practices. Time series of photosynthetically active radiation absorbed (APAR) by plants ($APAR_{plant}$) and soil ($APAR_{soil}$) were simulated with the DART radiative transfer model. First, realistic 3D models of the CA and AE fields were created and validated with a new method based on DART and Sentinel 2 and UAV reflectance and vegetation indices acquired in July 2019. At that date, around midday, $APAR_{plant}$ was larger by 21.5 W/m^2 in the AE field and $APAR_{soil}$ was larger by 20.1 W/m^2 in the CA field. We explained these differences by differences in geometric and optical parameters (OP) between the two fields. OP_{soil} causes ≈45% of the differences in $APAR_{plant}$ and $APAR_{soil}$. The shape of plant causes ≈14% of the difference in $APAR_{plant}$ and ≈17% in $APAR_{soil}$. OP_{plant} causes ≈14% of the difference in $APAR_{plant}$ and ≈1% in $APAR_{soil}$. Field geometry (row orientation, inter-row and plant distance) causes ≈7% of the difference in $APAR_{plant}$ and 2% in $APAR_{soil}$. It stresses the great role of OP_{soil} associated to AE practices. Because it integrates the non-linear effects of all above parameters, the LAI (Leaf Area Index) accounts for ≈40% difference in $APAR_{plant}$ and $APAR_{soil}$. The sensitivity of APAR to LAI is twice as low in the AE field than in the CA field. We showed that APAR differences between the AE and CA fields can be even greater with other maize row orientations. We also highlighted the role of the field model on simulated APAR by comparing the use of APAR simulated by a 3D field model and its corresponding 1D turbid field: 1D turbid models resulted in a 16% increase in $APAR_{plant}$ and in similar $APAR_{soil}$, compared to the 3D CA and AE models.

Nomenclature table:

AE field	field with agroecological practices
AE^M	AE field modified
APAR	Absorbed Photosynthetically Active Radiation
$APAR_{plant}$	Absorbed Photosynthetically Active Radiation for plant
$APAR_{soil}$	Absorbed Photosynthetically Active Radiation for soil
CA field	field with conventional practices
CA^M field	CA field modified

* Corresponding author.
E-mail address: paul.boitard@iut-tlse3.fr (P. Boitard).

https://doi.org/10.1016/j.rsase.2023.101079
Received 14 June 2023; Received in revised form 18 October 2023; Accepted 24 October 2023
Available online 27 October 2023

DART Discrete Anisotropic Radiative Transfer Model
MTD Mean Time Difference of $APAR_{plant}(t)$ or $APAR_{soil}(t)$ with time t from 11:00 to 14:
$00MTD^{*}_{plant}$ Mean Time Difference for plant = Mean $\left(APAR^{AE}_{plant}(t) - APAR^{CA}_{plant}(t)\right)$
MTD^{*}_{soil} Mean Time Difference for soil = Mean $\left(APAR^{AE}_{soil}(t) - APAR^{CA}_{soil}(t)\right)$
$MTD^{AEM\text{-}AE*}_{plant}$ Mean Time Difference for plant between AE field modified and AE reference
$MTD^{AEM\text{-}AE*}_{soil}$ Mean Time Difference for soil between AE field modified and AE reference
$MTD^{CAM\text{-}CA*}_{plant}$ Mean Time Difference for plant between CA field modified and CA reference
$MTD^{CAM\text{-}CA*}_{soil}$ Mean Time Difference for soil between CA field modified and CA reference
MTVI2 Modified Triangular Vegetation Index 2
NDVI Normalized Difference Vegetation Index
PAR Photosynthetically Active Radiation
RTM Radiative Transfer Model

1. Introduction

With 1,205,300 billion tons produced in 2021/2022 (U.S. Department of Agriculture), maize is the most cultivated cereal in the world. Knowing its radiative (Malenovský et al., 2021), hydric (Reddy et al., 2016; Walker and Ogindo, 2003; Brye et al., 2000) and energetic (Jankowski et al., 2020; Aquino Ferreira et al., 2018; Meyers and Hollinger, 2004) functioning is therefore of great importance and explains that it has already been the subject of numerous studies. The present pressure on water resources at a global scale, mainly due to global warming (IPCC, 2022: Impacts, Adaptation and Vulnerability, World Water development 2020), is leading to a review of certain agricultural practices, particularly irrigation. France is very concerned because it is the leading producer of maize in Europe and the fifth largest exporter worldwide (French Department of Agriculture). In addition, it is located in a climate transition zone with its Mediterranean rim particularly affected by the rise of the sub-Mediterranean climate (IPCC, 2022: Impacts, Adaptation and Vulnerability). Therefore, in France, maize irrigation is a major concern already extensively studied (Albert et al., 2021; Battude et al., 2017; Van der Velde et al., 2010). As a result, the number of irrigated areas in France has been decreasing in the past decade (Colas-Belcour et al., 2015). However, in Occitanie (southwest of France), one in four farms still uses irrigation and, maize is the leading irrigated crop with more than 150,000 ha (DRAAF 2018).

Instead of increasing water supply, various approaches can improve water availability: better water retention and infiltration in the soil, lower evaporation and better root exploration (Soltner, 2018). Past studies have shown the value of agroecological (AE) practices (Schoonhoven et al., 2018; De Benedetto et al., 2017), particularly for maize cultivation, both for soil conservation and evaluation of irrigation regimes (Hellin et al., 2013; Genet et al., 2022). For example, the Bag'Ages project (French acronym for "**B**assin **A**dour **G**aronne: quelles performances des pratiques **AG**roécologiqu**ES**"), commissioned by the Adour-Garonne water agency from 2016 to 2021, aimed to study the effect of AE practices (mainly no-till, cover cropping, and use of crop residues on soil surface) on water flows at the scale of the agricultural plot (BAGAGES 2021*)*. Here we consider one of the experimental sites, Estampes, of the Bag'Ages project that is part of the Regional Spatial Observatory (https://osr.cesbio.cnrs.fr) of CESBIO. It offers the advantage of two neighbour plots with different cultivation practices. One plot is cultivated with AE practices. The other plot is under conventional agriculture (CA) (Naylor, 1996) with deep mechanical ploughing, and more intensive use of chemical inputs (pesticides and synthetic fertilizers).

In the Estampes field, it has been observed that agroecological practices can reduce water usage in maize cultivation by approximately 20%. Additionally, these practices can have an impact on the in-canopy microclimate of monitored maize, resulting in an increase of 2 °C and a decrease of 10% relative humidity in the air over the growing period. It also highlighted that the herbicide nicosulfuron is more present in soil water with conventional agriculture practice (Cueff et al., 2021) and conventional agriculture is more likely to generate pesticide transfers (Cueff et al., 2020).

Understanding how AE practices influence thermo-hydric functioning is a major issue on a large scale. Many studies have assessed the contributions of AE practices on energy transfer (Gingrich et al., 2018), water management (Altieri et al., 2015) and temperature increase (Ofgeha and Abshire, 2021). Radiation absorption and emission in the short waves, called Radiative Budget (RB) here, greatly influences thermo-hydric functioning. A major challenge that defines our study in the continuity of the Bag'Ages project is to quantify the RB differences due to AE and CA practices. More specifically, we consider the impact of soil and plant optical properties, shape of maize plant, field geometry (row orientation, inter-row and plant distance) and LAI on Absorbed Photosynthetic Active Radiation (APAR: 0.4–0.7 μm) as it is the main source of energy for vegetation functioning.

We used UAV and satellite images in the visible and near infrared range (i.e., short waves) as well as in situ measurements of the Bag Ages project. For studying the time evolution of APAR and how it depends on the geometry and optical properties of the maize field we needed a 3D radiative transfer model (RTM) adapted to short waves. Previous studies have shown the usefulness of 3D RTMs, especially for investigating the effects of vegetation clumping (Duthoit et al., 2008) and 3D architecture. More recently, researchers have increasingly used these models to explore the impact of plant shape and shading (Wen et al., 2019, 2021). A few short wave 3D RTMs exist such as DART (dart.omp.eu), MCScenes (spectral.com/our-software/mcscene), LESS (lessrt.org), DIRSIG (dirsig.cis.rit.edu /docs/new/intro.html), FLIGHT (flight-rtm.github.io) and WPS (Zhao, 2015). We chose DART here as it is one of the most complete

3D RTMs (Wang et al., 2022) and one of the most accurate 3D RTMs in the RAMI experiment (Widlowski et al., 2015). In addition, it has been used in many vegetation studies (Sepulcre-Cantó et al., 2009; Sobrino et al., 2011; Hernández-Clemente et al., 2012; Wei et al., 2020; Malenovský et al., 2021).

In this work, we designed a new methodology that creates a 3D model of maize fields from UAV and satellite reflectance (green, red, NIR) and vegetation indices images. This so-called "DART calibration" allowed us to study how APAR changes with time, and which geometric and optical properties condition it. To do so, we used DART to create a 3D model of spatially distributed maize plants made of facets (i.e., triangles), with the constraint of correct LAI per field (LAI_{DART}). LAI is often derived from satellite images (e.g., Sentinel 2) using inversion methods (Brede et al., 2020) whose accuracy depends on many factors including the field geometry, the shape of the maize plants and the optical properties of the soil (OP_{soil}) and maize plants (OP_{plant}). Here, we used the Sentinel-2 (S2) LAI product derived by processing S2 reflectance images with the SNAP (LAI_{SNAP}) tool (Sentinel Application Platform: https://earth.esa.int/eogateway/tools/snap). However, studies (Kganyago et al., 2020) already showed that LAI_{SNAP} and mean in situ LAI (collected by LICOR 2200 c Plant Canopy Anal) can greatly differ on maize field with RMSE > 2 m^2. m^{-2}. Therefore, we developed another method to adjust the LAI_{DART} according to the reflectance and vegetation indices S2 and UAV. LAI has already been derived from satellite reflectance images using DART models (Jiang et al., 2022). The work presented in this paper differs from previous studies in three ways:

1) Creation of 3D maize field model with realistic atmospheric spectral radiance.
2) Innovative calibration of the 3D maize fields (i.e., assignation of OP_{soil}, OP_{plant} and LAI) using UAV and satellite reflectance images with fixed LAI_{SNAP} or adjusted LAI.
3) Sensitivity studies on the plant and soil hourly APAR, stressing differences between AE and CA practices, and quantifying the effect of various optical and geometrical factors.

Section 1 presents the study site, in-situ, UAV and satellite data, and the DART model. Section 2 describes the methods used to create, calibrate and validate the field 3D models used by DART, and also to conduct sensitivity studies with these 3D models. Section 3 details the results on LAI determination and sensitivity studies on APAR. Section 4 discusses the DART 3D model spatialization, the impact of the maize row's orientation and a comparison of 1D and 3D models of the maize field. Finally, Section 5 presents conclusions and future works.

2. Data and methods

2.1. Studied site

Our work took place on July 2019, at a time when maize growth stage is well suited to its satellite observation. The Estampes study site (43°41′N; 0°28′E, altitude = 266 m) has an oceanic climate, according to the Köppen climate classification. It is in the Boués catchment in the Gers region, south west France. Cueff et al., (2020),2021 classified the soil on the site as Stagnic Luvisol according to the World Reference Base for Soil Resources (IUSS Working Group WRB, 2007), which corresponds to Luvisol redoxisol in the French Soil Classification (AFES, 2008), locally called "Boulbènes". It has a loamy surface layer (fine and coarse silt ≈ 450–500 g/kg) and an illuvial clay horizon from 45 to 55 cm. Due to these properties, especially hydromorphic conditions at low depth, this soil has a moderate agronomic potential with mainly irrigated crops.

The site (Fig. 1) consists of two neighbour plots under CA and AE practices with an East-West orientation of maize rows (i.e., 270° N field orientation). This orientation is predominant in the Gers (Fig. 2) due to a repetitive landscape of hillsides and north-south valleys downstream from the Pyrenean Mountain chain. The two plots have a slight slope, similar surfaces (≈10 ha) and sowing density, with different inter-rows and inter-plants distances. For more than 40 years, the CA plot was cultivated in soybean–maize rotation, with soil left bare in winter and plowed with a moldboard to a depth of 30 cm. Since 2000, the AE plot is managed with crop maize-soybean rotation including sometimes wheat and cover cropping, permanent mulch on the soil surface, and no-tillage.

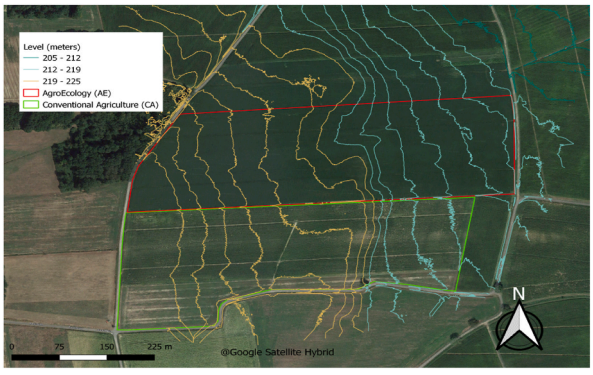

Fig. 1. Google image with topography (yellow, blue) and CA and AE field boundaries (red, green). (For interpretation of the references to colour in this figure legend, the reader is referred to the Web version of this article.)

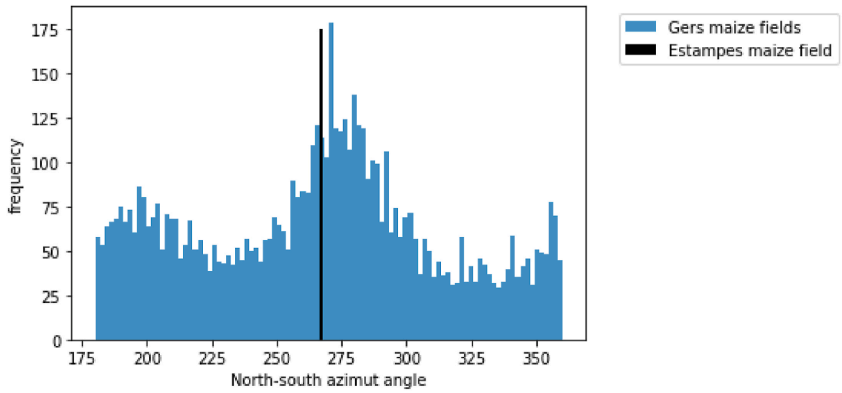

Fig. 2. Maize fields orientation in the Gers area in 2019 (internal technical note Lab'OT CNES, https://eolab.cnes.fr/projets/orientation-des-cultures-agricoles).

2.2. *In situ data*

The dataset used in this study is based on different types of measurements.

- 4-component radiation instrument (NR01). It was installed on a mast at a height of 3m in each field. Its two CM3 pyranometers measured short waves ([0.3–3 μm]), one measuring the downward incident solar radiation and the other measuring the upward reflection of solar radiation. Its two CM3 pyrgeometers measured long waves ([3–100 μm]), one measuring downward TIR radiation from the atmosphere and the other measuring upward TIR radiation from the earth's surface.
- Average plant height (CA ≈ 2m, AE ≈ 1.6m), number of leaves (10), distances between rows and plants per field. Unlike the AE field, the CA field has well-marked rows because its inter-row spacing is much greater than its inter-plant distance.
- ASD field spectroradiometer (www.malvernpanalytical.com) FieldSpec 4 from 0.35 to 2.5 μm. On July 11, 2019 we measured eight OP_{plant} spectra and three OP_{soil} spectra at different locations in each field (Fig. 3).
- Thermal camera (Optris) at a height of 7 m. It provided thermal infrared images of the 2 fields.
- Weather station between the two fields. In July 2019, on average, the air temperature was 24 °C, the relative humidity was 75%, and the daily irradiance over [0.3–3 μm] was 250 W/m^2.
- ibutton micro sensors. They measured soil temperature and also air temperature and relative humidity in the canopy.

2.3. *Satellite data*

The Copernicus Sentinel-2 mission consists of two identical satellites in the same orbit, S2A and S2B, launched by the European Space Agency in 2015 and 2017, respectively. It aims to provide comprehensive and up-to-date data for environmental monitoring. Each satellite carries a wide swath high-resolution multispectral imager with 13 spectral bands. Here, we used the S2B image of 10/07/2019 at 11:00 a.m., provided by the THEIA platform (https://www.theia-land.fr/product/reflectance-de-surface-sentinel-2) at

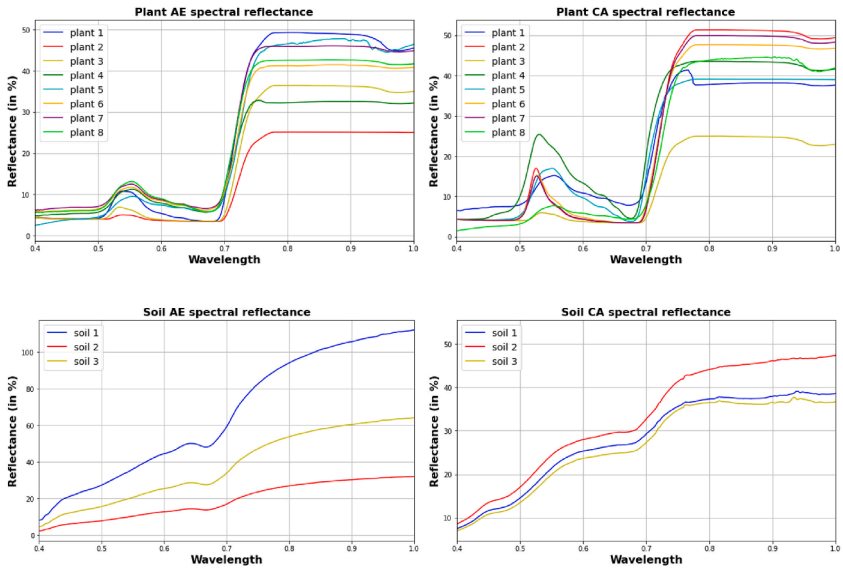

Fig. 3. OP_{plant} and OP_{soil} from AE and CA field function of wavelength obtained with ASD field spectroradiometer.

level 2A with an atmospheric correction based on multi-temporal information. Many studies on maize have already been conducted with S2 images (Ren et al., 2020; Fan et al., 2020). Here, in addition to LAI_{SNAP} we used the green, red, and NIR reflectance images, and NDVI and MTIV2 vegetations index images. These indices were chosen because NDVI is a major vegetation index, particularly for estimating LAI, and MTVI2 gives better results when NDVI saturates (Smith et al., 2008):

$$NDVI = \frac{\rho_{NIR} - \rho_{Red}}{\rho_{NIR} + \rho_{Red}} \quad (1)$$

$$MTVI2 = \frac{1.5\ [1.2\ (\rho_{NIR} - \rho_{Green}) - 2.5\ (\rho_{Red} - \rho_{Green})]}{\sqrt{(2\ \rho NIR + 1)^2 - \left(6\ \rho_{NIR} - 5\ \sqrt{\rho_{Red}}\right) - 0.5}} \quad (2)$$

2.4. UAV images

Airborne UAVs are commonly used in precision agriculture for monitoring vegetation health and crop growth, yield estimation (Nebiker et al., 2016), vegetation cover mapping, species classification (Laliberte et al., 2011) and plant phenotyping (Sagan et al., 2019), chemical spraying optimization and surface condition characterization (Raeva et al., 2019). On 11/07/2019 at 12:00 UTC, a multiSPEC 4C camera on a Fly eBee Classic UAV acquired red, green, red-edge and NIR images of the two fields at 11.66 cm spatial resolution (Table 2 .). Twenty minutes of flight led to 1200 images with a 90% overlap in order to ease stereoscopic analysis. The GE-ODE laboratory (https://geode.univ-tlse2.fr) geometrically and radiometrically transformed them into orthorectified mosaic reflectance images using the Pix4Dmapper and PhotoScan AgiSoft software (Raeva et al., 2019) while considering the UAV motion, propeller vibration, scene wind and relief.

NDVI and MTVI2 vegetation indices and a soil vegetation classification map of the two fields at 3 cm resolution were derived from the UAV reflectance images (Marais-Sicre et al., 2023). We used them to select the vegetation and soil pure pixels in the UAV spectral images of the two fields.

2.5. DART

DART simulates the RB and remote sensing (RS) observations (VIS / TIR spectro-radiometer, LiDAR) of natural and urban surfaces. It has been developed at CESBIO since 1992 and was patented in 2003. It contains the PROSPECT and FLUSPECT (Feret et al., 2008) leaf models, and the MARMIT (Dupiau et al., 2022) soil model. It has two modes. 1) DART-FT (Gastellu-Etchegorry et al., 1996): its iterative discrete ordinate method tracks radiation in a finite number of directions (e.g., 100), in a voxelized scene. 2) DART-Lux (Wang et al., 2022): its bidirectional Monte Carlo method launches photons from the radiation sources and the sensor in a non voxelized scene. DART imports and creates scenes as the spatial distribution of 3D scene elements (e.g., 3D maize plant) either imported or directly created by DART. In this study the DART-FT is used in order to compute the radiative budget.

3. Methodology for creating the 3D DART scenes

3.1. Characteristics of the 3D scenes

A DART scene is mostly defined by a spectral illumination and a distribution of scene elements with specific optical properties:

- Sun direction. The DART sun calculator computed it at the date of UAV and S2 observations.

Table 1
Information on the CA and AE fields in 2019.

Cultivation practices	CA field	AE field
Maize variety	Maize grain PR934	Maize grain P0900
Area	9,3 ha	10.4 ha
Planting - Harvest date	29/03/2019–21/10/2019	30/04/2019–19/10/2019
Planting density	80 000 plants/ha	90 000 plants/ha
Geometry fields	Inter-rows: 0.8m. Inter-plants: 0.125m	Inter-rows: 0.4m. Inter-plants: 0.25m

Table 2
Information on UAV EBEE and satellite S2 used for this study.

Sensor	Band	Wavelength	Bandwidth
Satellite S2B / MSI (10 m resolution)	Blue	492.1 nm	98 nm
	Green	559 nm	46 nm
	Red	665 nm	39 nm
	Near infrared	833 nm	133 nm
UAV Ebee / Multi Spec 4 C (11.6 cm resolution)	Green	550 nm	40 nm
	Red	660 nm	40 nm
	Red Edge	735 nm	10 nm
	Near infrared	790 nm	40 nm

- Spectral illumination. The APAR simulation requires knowledge of the spectral illumination of maize fields, whereas only broadband PAR irradiance was available. Therefore, to obtain it, we used a two-step approach. 1) Derivation of the spectral optical depth of aerosols and clouds from irradiance measured in-situ (cf. 1.2) at the time of the UAV and S2 observations. This inversion was done using the DART atmosphere radiance transfer module with the Mid-Latitude Summer gas model and Rural aerosol model. 2) DART simulation of BOA irradiance per UAV and S2 and for the eight spectral band using the aerosol and cloud optical depth computed in 1).
- Spectral bands. Depending on the objective of the work, different spectral bands are input such as the spectral bands of S2 and UAV (Table 2) for comparison of DART simulations and S2 or UAV data.
- 3D maize plants in CA and AE fields. We created them using the 3D creation suite Blender (www.blender.org) with photos and measurements of plants in the CA and AE fields (Fig. 4).
- 3D models representative of the CA and AE fields. We created them in DART, using inter-row and inter-plant distances, plant spatial variability and azimuthal variability over [-20°, +20°] measured per field (Table 1). We choose models with 1 m^2 area, each with 10 identical maize plants infinitely duplicated by DART (repetitive mode) in order to simply extend the model area and save the computing time.
- LAI_{DART}. DART sets it by scaling 3D object elements along the x, y and z axes. LAI_{DART} was initially set to the median value of LAI_{SNAP}.
- OP_{soil} and OP_{plant}. They were derived from the soil and plant spectra measured in the field by ASD field spectroradiometer (Fig. 3). OPs have spatially constant values in each field model. For each field, we have 24 possible combinations of pairs (OPsoil, OPplant).

3.2. Calibration and validation methods of the CA and AE models

The objective is to create statistically representative DART maize models capturing the median majority case, aligning with the reflectance and vegetation indices for each field. The calibration of the field models (i.e., assignation of OP_{soil}, OP_{plant} and LAI to the 3D models) was done with a method that minimizes differences between DART simulation and median values of:

- UAV or S2 green, red and NIR reflectance (MR) to the respective resolutions. The other bands of S2 and UAV have not been taken into account, as they are not common to both sensors and therefore do not allow the "S2, UAV, DART" comparison.
- vegetation indices NDVI and MTVI2 (MVI) at 10 m resolution by resampling the UAV's images to keep the same usual representativeness for VI.

The reflectance and VI differences are noted Δ^{S2}_{MR}, Δ^{UAV}_{MR}, Δ^{S2}_{MVI} and Δ^{UAV}_{MVI}, respectively. In order to minimize this equifinality issue, we designed two DART calibration methods to assess the OP_{soil}, OP_{plant} and LAI of the field models:

a) **Fixed LAI_{SNAP}** (Fig. 5). The 4-step calibration method sets the LAI of each field as the median value of LAI_{SNAP} (Fig. 7) and computes Δ^{S2}_{MR} (green, red and NIR bands) and Δ^{S2}_{MVI} (NDVI and MTIV2) for all possible pairs (OP_{soil}, OP_{plant}) measured in the field. It selects the pair that gives the minimum Δ^{S2}_{MR} and Δ^{S2}_{MVI} values.

b) **LAI adjustment** (Fig. 6). The 7-step calibration method varies LAI in a range defined by modifying the leaf area of 3D plants through the application by DART of x,y,z scaling factors to the 3D plants. Methods commonly used to estimate LAI rely on either reflectance (Jiang et al., 2022) or NDVI (Bajocco et al., 2022). However, due to uncertainties and equifinality, different combinations of OP and LAI values can produce the same reflectance or vegetation index. To solve this problem, the methods proposed in this study use both vegetation indices and reflectance to provide a more accurate estimation of LAI. We choose to calculate two LAI values as follow:
   - LAI_1: it minimizes Δ^{S2}_{MR} or Δ^{UAV}_{MR}, in red, green and NIR bands for pixels whose VI belongs to the interval [0.98 x Median VI 1.02 x Median VI] in the VI images (Fig. 8).
   - LAI_2: it minimizes differences of DART with S2 (Δ^{S2}_{MVI}) or UAV (Δ^{UAV}_{MVI}) vegetation indices.

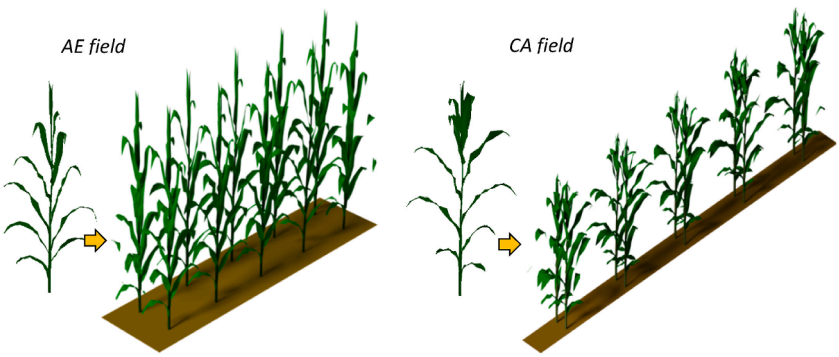

Fig. 4. 3D models of the AE (left) and CA (right) maize plants and fields.

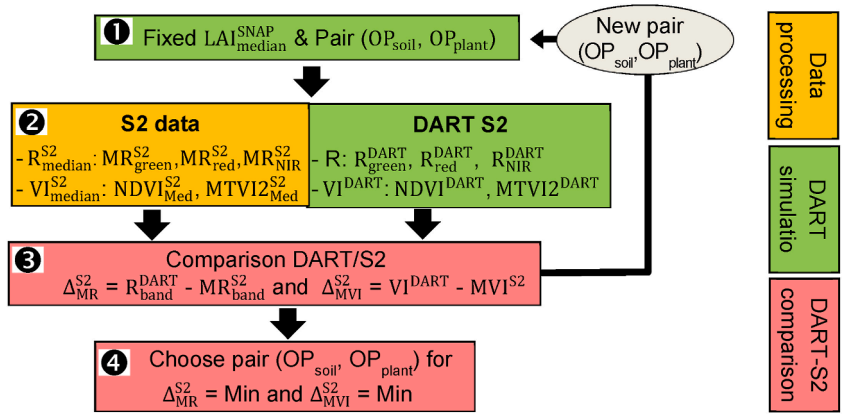

Fig. 5. Algorithm of the calibration method to get (OP$_{soil}$, OP$_{plant}$) with fixed LAI$_{SNAP}$. R stands for reflectance and VI for vegetation index.

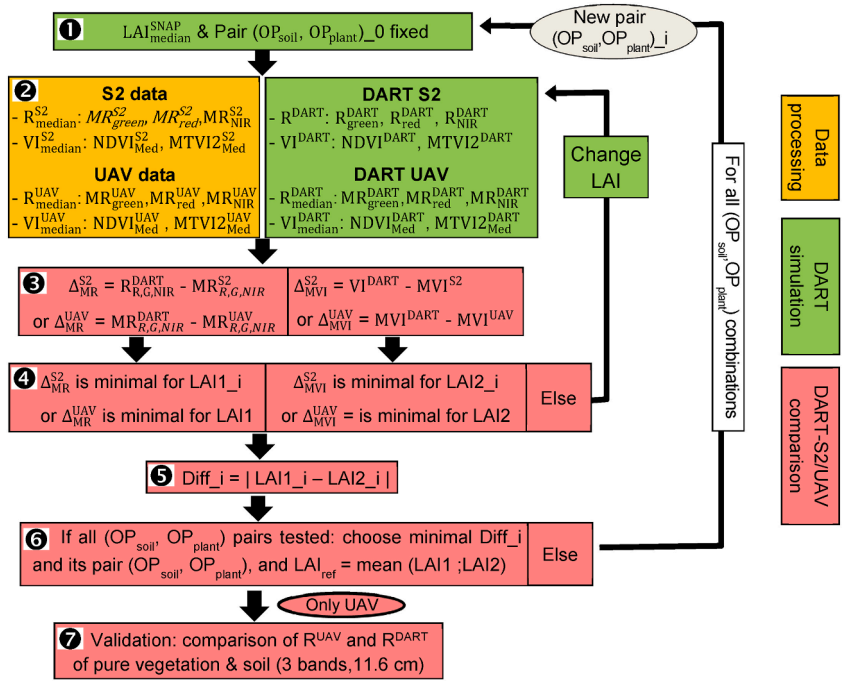

Fig. 6. Algorithm of the calibration method to get LAI using measured (OP$_{soil}$, OP$_{plant}$).

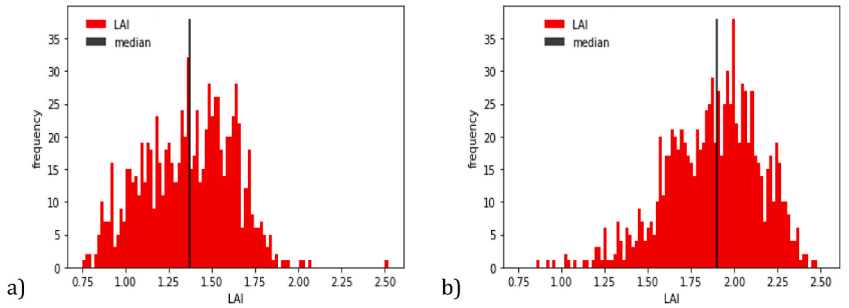

Fig. 7. Histograms and median values of LAI$_{SNAP}$ at 10 m resolution for the CA (a) and AE (b) fields. 955 pixels for the AE field and 873 pixels for the CA field.

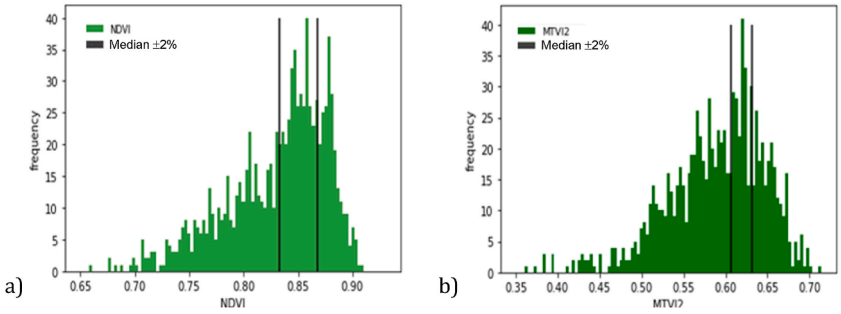

Fig. 8. Histograms of NDVI (a) and MTVI2 (b) pixels of the AE field in the UAV image resampled at 10 m resolution. The interval [0.98 x Median VI 1.02 x Median VI] contains 333 pixels (34.8%) for NDVI and 196 pixels (20.5%) for MTVI2.

The selected pair (OP_{soil}, OP_{plant}) gives Diff = $|LAI_1 - LAI_2|$. These operations are repeated for all possible combinations of the database. When all combinations have been tested, the combination with the minimum Diff is chosen and the LAI_{DART} become LAIref = $\frac{LAI_1+LAI_2}{2}$. The objective is to verify if there is a common convergence between the two approaches R and VI corresponding to a global min Diff for the same combination of OP.

For UAV data, the validity of the two models fields was tested by comparing the reflectance of pure plant and soil pixels in the DART and UAV images. We used a k-means classification based on soil and vegetation indices calculated on UAV RGB images to separate plant and soil (Marais-Sicre et al., 2023).

3.3. Sensitivity analysis on PAR absorption

In this study we focus on APAR because it is the energy conditioning plant physiology in the short wavelengths. We studied the $APAR_{plant}$ and $APAR_{soil}$ (Fig. 9) when solar irradiance is maximal, from 11:00 to 14:00 UTC on 11/07/2019 by steps of 10 min, with the objective to quantify:

- The differences in APAR between AE and CA fields.
- The influence of the field geometry and optical properties (OP_{soil} and OP_{plant}) on APAR.
- The impact of maize row orientation relative to sun direction on APAR.
- The influence of plant model simulated as 3D objects or 1D turbid on APAR.

To simulate the APAR with DART, we sampled the PAR domain with eight contiguous spectral bands. Table 3 shows the central wavelength and bandwidth of each band. This specific band configuration was determined through a sensitivity study (not detailed here), which revealed that the difference in APAR simulated with eight bands compared to twenty bands was less than 1%.

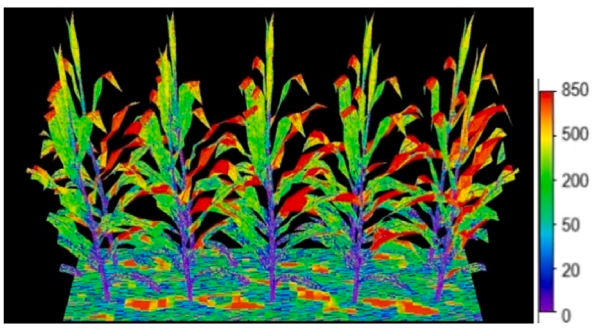

Fig. 9. DART simulated APAR (W/m^2) of the AE field 11/07/2019 at 11 a.m.

Table 3
Central wavelength $\bar{\lambda}$, bandwidth $\Delta\lambda$ of the eight DART spectral bands used to compute APAR.

DART band	band 1	band 2	band 3	band 4	band 5	band 6	band 7	band 8
$\bar{\lambda}$ (μm)	0.419	0.456	0.493	0.531	0.568	0.606	0.643	0.681
$\Delta\lambda$ (μm)	0.037	0.037	0.037	0.037	0.037	0.037	0.037	0.037

4. Results

4.1. LAI inversion and validation

The DART calibration method "fixed LAI_{SNAP}" could not provide a pair (OP_{soil}, OP_{plant}) that verifies both reflectance and VI criteria. Some pairs (OP_{soil}, OP_{plant}) led to minimal Δ_{MR} but with delta-VI larger than 35%. The calibration method "LAI adjustment" led to realistic LAI values: $LAI_{AE} = 3.2$ (m2/m2) and $LAI_{CA} = 2.8$ with S2 data, and $LAI_{AE} = 3.5$ and $LAI_{CA} = 3.2$ with UAV data. These LAI values meet the validation requirements:

- similar VI values of DART compared to S2 and UAV (Table 4.) at 10 m.
- DART green, red and NIR reflectances was in the range of UAV and S2 reflectances and close to its median values, usually between the first and third quartiles (Fig. 10).

This comparison was done using UAV and S2 pixels where VI values were within 2% of the median value of the VI_{S2} and VI_{UAV} images for each field. Results call then into question the accuracy of LAI_{SNAP} for 3D simulation, as already noted by Kganyago et al., (2020) who showed differences (RMSE $> 2\ m^2\ m^{-2}$) between LAI_{SNAP} and in situ mean LAI (measured LICOR 2200 c Plant Canopy Anal) with LAI values close to our study. Indeed, SNAP computes the LAI with a radiative transfer model that treats vegetation as a homogeneous turbid volume (Weiss et al., 2020) which is not adapted to vegetation canopies with a well-marked 3D architecture.

Below, the calibration based on LAI adjustment with UAV data (see 2.2)b)) is used because:

- Δ_{MR}^{UAV} and Δ_{MVI}^{UAV} are smaller than Δ_{MR}^{S2} and Δ_{MVI}^{S2}.
- DART green, red and NIR reflectance is in the range of UAV reflectances, with close median values (Fig. 9). It stresses a good statistical representation of the DART field compared to the UAV data. The comparison of DART and S2 reflectance could be compared on only one value, because the 3D field model was smaller than the S2 pixels. However, Fig. 10 shows that DART green, red and NIR reflectance values are also close to S2 reflectance values, but less than for UAV.
- DART and UAV vegetation indices are close, with larger difference less than 5 % (Table 4.).
- The 3D models of the fields could be successfully tested with close reflectance of pure vegetation and soil pixels in the DART and UAV images (Fig. 11).

4.2. Determinants of APAR

4.2.1. Differences in APAR between CA and AE fields

The micro-climate (e.g., air in canopy and soil temperature and humidity) differs between the CA and AE fields, as shown by field measurements (Bag'Ages project 2021). In order to assess differences in APAR between the two fields, we computed mean time differences (MTD) of $APAR_{plant}(t)$ and $APAR_{soil}(t)$ with time t from 11:00 to 14:00 on July 11, 2019 between the two fields: $MTD^{*}_{plant} = \text{Mean}\left(APAR^{AE}_{plant}(t) - APAR^{CA}_{plant}(t)\right)$; $MTD^{*}_{soil} = \text{Mean}\left(APAR^{AE}_{soil}(t) - APAR^{CA}_{soil}(t)\right)$. The symbol * indicates that MTD* is for the realistic case (i.e., calibrated 3D field models). Fig. 12 shows $APAR^{CA}_{plant}(t)$ and $APAR^{AE}_{plant}(t)$. Their values, and shapes to a lesser extent, differ with positive $MTD^{*}_{plant} \approx 21.5\ W/m^2$ and negative $MTD^{*}_{soil} \approx -20.1\ W/m^2$. The main causes of APAR differences between the fields are presented below. The influencing parameters have been tested one by one in order to quantify the impact of each. Each

Table 4
DART, S2 and UAV NDVI and MTVI2 for the AE and CA fields.

Vegetation indices	AE field	CA field
NDVI median UAV	0.86	0.85
NDVI median S2	0.83	0.76
NDVI DART for UAV	0.86	0.85
MTVI2 median UAV	0.57	0.66
MTVI2 median S2	0.60	0.58
MTVI2 DART for UAV	0.58	0.63

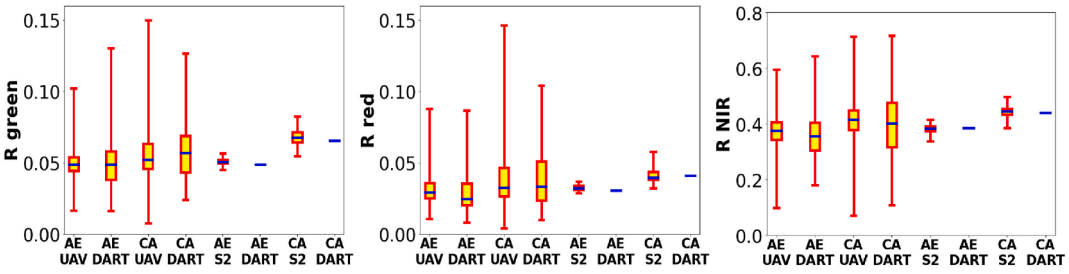

Fig. 10. UAV, S2 and DART reflectance green (left) / red (middle) / NIR (right) of the AE and CA fields on 11 July at 2pm for UAV and 10 July at 11am for S2. For each field DART simulations are for the 3D field model calibrated either with UAV or S2 data. (For interpretation of the references to colour in this figure legend, the reader is referred to the Web version of this article.)

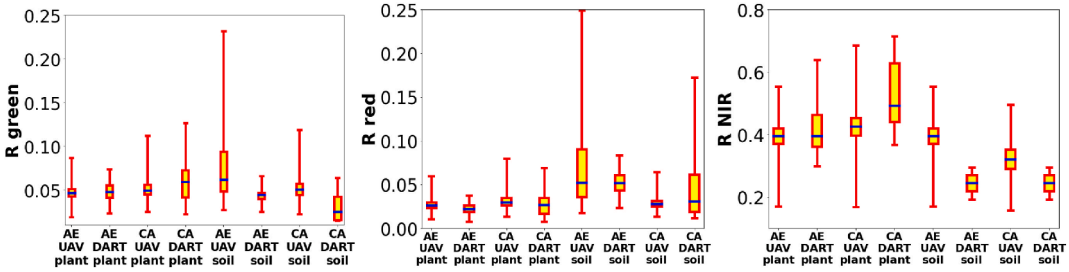

Fig. 11. UAV and DART green (left) / red (middle) / NIR (right) reflectance of pure vegetation (plant) and soil pixels for the AE and CA fields. (For interpretation of the references to colour in this figure legend, the reader is referred to the Web version of this article.)

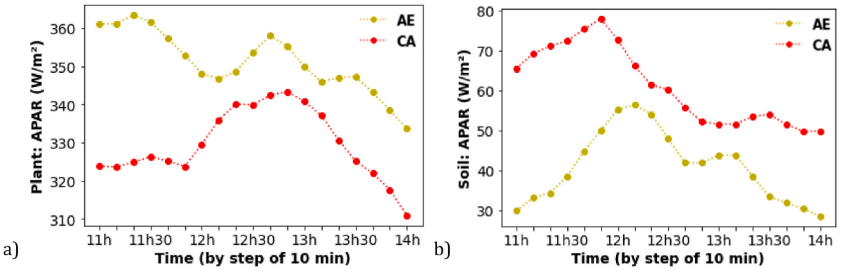

Fig. 12. $APAR_{plant}(t)$ (left) and $APAR_{soil}(t)$ (right) of the AE and CA fields.

CA parameter (geometry field, shape of plant, OP soil and plant, LAI) was assigned one by one to the AE field and vice versa, all other parameters remaining unchanged. It led to two modified models of AE and CA fields per case. In the rest of the study the field models AE and CA that have been modified with a parameter of the other field will be noted AE^M and CA^M.

4.2.2. Soil and plant optical properties

OP_{soil}^{AE} and OP_{soil}^{CA} greatly differ because the AE and CA soils have different agricultural practices, especially with crop residues and no-till in the AE field. Fig. 13 shows that the modified AE field with OP_{soil}^{CA} compared to the real AE field has $MTD_{plant}^{AEM\text{-}AE*} = -8.9$ W/m^2 and $MTD_{soil}^{AEM\text{-}AE*} = 9.7$ W/m^2. The modified CA field with OP_{soil}^{AE} compared to the real CA field has $MTD_{plant}^{CAM\text{-}CA*} = 9.8$ W/m^2 and $MTD_{soil}^{CAM\text{-}CA*} = -11.6$ W/m^2. It is consistent with the fact that the soil of the AE field reflects much more radiation to the plants than the soil of the CA field. These results show that OP_{soil} accounts for almost half of MTD_{soil}^{*} (-20.1 W/m^2) and MTD_{plant}^{*} (21.5 W/m^2).

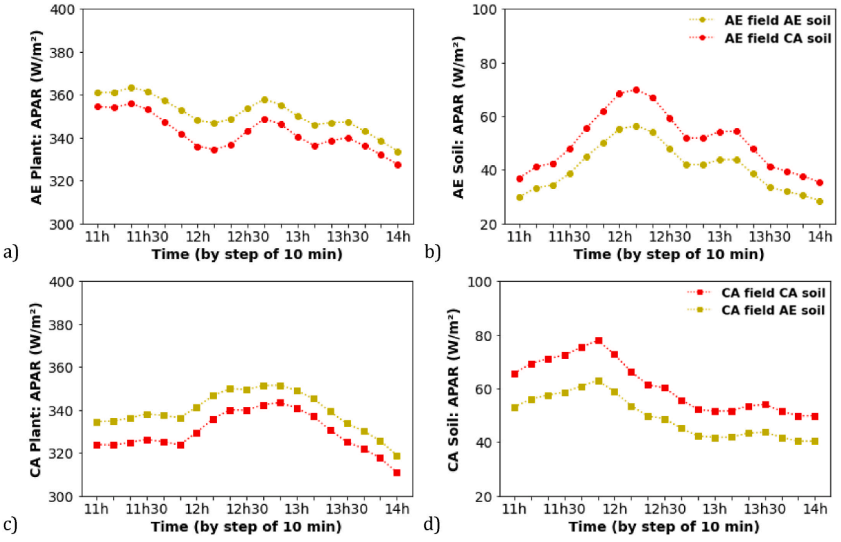

Fig. 13. $APAR_{plant}(t)$ (a,c) and $APAR_{soil}(t)$ (b,d) of AE (a,b) and CA (c,d) fields with OP^M_{soil}.

Being very close, OP^{CA}_{plant} and OP^{AE}_{plant} only slightly influence MTD_{plant} and MTD_{soil}. Therefore, swapping them between the CA and AE fields only slightly changes their $APAR_{plant}$, and even much less their $APAR_{soil}$. For example, $MTD^{AEM\text{-}AE*}_{plant} = -3.1$ W/m² in the AE field modified with OP^{CA}_{plant}.

4.2.3. Field geometry and plant shape

Row and plant spacing (Table 1), called "field geometry", can influence APAR. Fig. 14 shows $APAR_{plant}(t)$ and $APAR_{soil}(t)$ of the AE and CA fields with swapped row and plant spacings, with LAI remaining constant. Their changes are positive or negative depending on time t. Their mean change is very low for the AE field ($MTD^{AEM\text{-}AE*}_{plant} = -1.5$ W/m², $MTD^{AEM\text{-}AE*}_{soil} = 0.6$ W/m²) and larger for the CA field ($MTD^{CAM\text{-}CA*}_{plant} = 5.3$ W/m², $MTD^{CAM\text{-}CA*}_{soil} = -5.1$ W/m²).

We also studied how the shape of the 3D models of the CA and AE maize plants influence $APAR_{plant}$ and $APAR_{soil}$. The swap of plant models between the CA and AE fields, with LAI remaining constant, led to: $MTD^{AEM\text{-}AE*}_{plant} = -3.9$ W/m², $MTD^{AEM\text{-}AE*}_{soil} = 3.9$ W/m², $MTD^{CAM\text{-}CA*}_{plant} = 2.9$ W/m² and $MTD^{CAM\text{-}CA*}_{soil} = -3.7$ W/m². Therefore, compared to the CA_{plant}, the AE_{plant} leads to higher $APAR_{plant}$ and smaller $APAR_{soil}$.

As a consequence, AE geometry and plant combine their effects in favour of $APAR_{plant}$ If LAI increases (not shown here), the difference in $APAR_{plant}$ in favour of AE_{plant} increases.

4.2.4. LAI

LAI is a key factor for $APAR_{plant}(t)$ and $APAR_{soil}(t)$. The DART calibration gave close LAI values for the two fields: $LAI_{AE} = 3.5$ m²/m² and $LAI_{CA} = 3.2$ m²/m². In order to study the impact of LAI on APAR(t), we created 3D models of CA and AE fields with equal LAI (i.e., $LAI_{AE} = 3.2$ and $LAI_{CA} = 3.5$) while keeping their other parameters (*e.g.*, real plant spatial distribution). Fig. 15 shows that if the two fields have the same LAI, their mean APAR becomes closer but still differs: $MTD_{plant} = 8.2$ W/m² for $LAI_{CA} = LAI_{AE} = 3.2$ and $MTD_{plant} = 10.5$ W/m² for $LAI_{CA} = LAI_{AE} = 3.5$, whereas $MTD^{*}_{plant} = 21.5$ W/m² for the real case. Results are similar for the soil: $MTD_{soil} = -7.9$ W/m² for LAI = 3.2 and $MTD_{soil} = -9.1$ W/m² for LAI = 3.5, whereas $MTD^{*}_{soil} = -20.1$ W/m². It stresses that LAI explains slightly less than 50% of differences in $APAR_{soil}$ and $APAR_{plant}$.

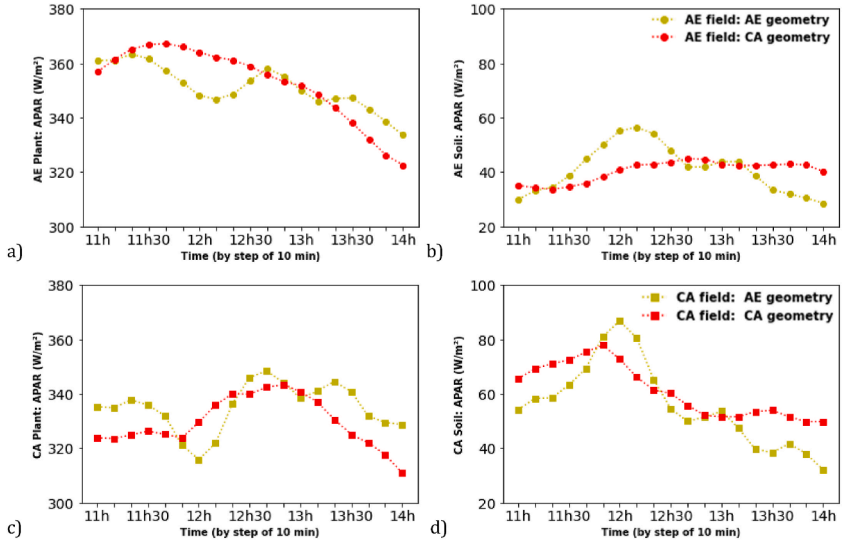

Fig. 14. $APAR_{plant}(t)$ and $APAR_{soil}(t)$.

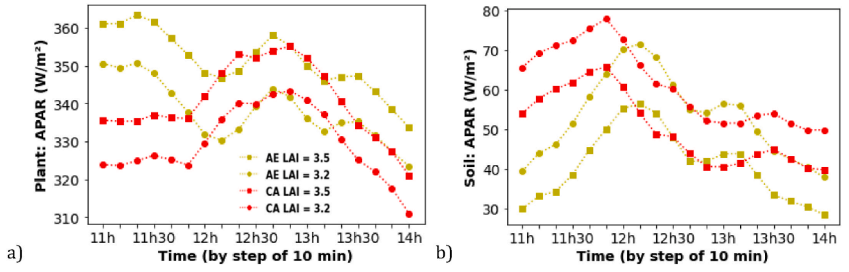

Fig. 15. $APAR_{plant}(t)$ (a) and $APAR_{soil}(t)$ (b) of AE and CA fields with same LAI (*i.e.*, 3.2 and 3.5).

To better understand the influence of LAI, we simulated how a variation ΔLAI from −2 to +2 around the real case influences $APAR_{plant}$ and $APAR_{soil}$. Fig. 16 shows $\Delta APAR^{AE}_{plant}$ (ΔLAI), $\Delta APAR^{AE}_{soil}$ (ΔLAI), $\Delta APAR^{CA}_{plant}$ (ΔLAI) and $\Delta APAR^{CA}_{soil}$ (ΔLAI). It stresses that $APAR_{plant}$(LAI) and $APAR_{soil}$(LAI) are non-linear with very different slopes (i.e., sensitivity of APAR to LAI) around the real case. Slopes are positive for $APAR_{plant}$ and almost two times higher for CA than for AE. They are negative for $APAR_{soil}$ and larger for CA than for AE. Therefore, the small shift of LAI between AE (3.5) and CA (3.2) has a greater impact on $APAR^{CA}$: for the LAI values, the geometric factors (field geometry, shape of plant) have a larger influence on APAR in the CA field than in the AE field. These results are consistent with the fact that an increase of LAI implies a lower sensitivity of ΔAPAR to ΔLAI.

5. Discussion

5.1. 3D DART field model spatialization

This work was conducted using 3D models with LAI and OP values derived from median values of satellite and UAV reflectance and vegetation indices. This simplified approach saved simulation time and computer memory. However, it necessarily introduces some inaccuracy. In the future, this model could be spatially distributed to represent spatial heterogeneity across the field using UAV or satellite data. We will also consider the local topography.

5.2. Row orientation

We investigated the role of row orientation because it influences the APAR and remote sensing observations of vegetation (Gastellu-Etchegorry et al., 2017). Fig. 17 illustrates the change of $APAR_{plant}(t)$ and $APAR_{soil}(t)$ of the CA and AE fields for the four orientations. Due to symmetry considerations, we considered only 30°, 60° and 90° rotations relative to the actual East-West orientation (section 1.1), which corresponds to 0° rotation. Compared to the real case, the time average of absolute $\Delta APAR^{AE*-AE}$ ranges from 1.6 to 12.7 W/m^2, whereas absolute $\Delta APAR^{CA*-CA}$ ranges from 6.8 to 15.9 W/m^2. The larger role of row orientation for the CA field is consistent with the fact that row spacing in the CA field is twice as large as in the AE field. The real row orientation (i.e., 0° rotation) gives the smaller $APAR_{plant}$ and larger $APAR_{soil}$ for the AE field, and the larger $APAR_{plant}$ and smaller $APAR_{soil}$ for the CA field. Table 5 shows the MTD between CA and AE for the four rotations. MTD_{soil} is always positive and MTD_{plant} is always negative for all row rotations. The difference in $APAR_{plant}$ and $APAR_{soil}$ between AE and CA fields remains regardless the orientation of fields. MTD_{plant} and MTD_{soil} are minimal for the real case (sun direction perpendicular to the maize rows at noon) and are extreme with sun direction parallel to the maize rows at noon (i.e., 90° rotation). Therefore, the real row orientation minimizes the difference between both fields.

As a consequence, the actual row orientation minimizes the difference between both fields. From a theoretical and modelling point of view, AE plant could still win APAR with another row orientation by maximizing it for 90°. Fig. 2 indicates that 0° and 90° are the most frequent directions in the study area.

5.3. Comparison 1D/3D

Models commonly represent vegetation as the superimposition of homogeneous layers filled with turbid medium (*e.g.*, SCOPE, Yang et al., 2021) to simulate the RB of vegetation, including the APAR. Indeed, this 1D model of vegetation requires little simulation time and few parameters. However, it is a major source of error on the estimate of APAR. This is investigated here for the two maize fields through the creation of 1D models of the CA and AE fields as superimposed homogeneous and horizontal layers of turbid medium, using the parameters of the 3D models (plant height, OP, …). Fig. 18 shows the $APAR_{soil}(t)$ and $APAR_{plant}(t)$ of the AE and

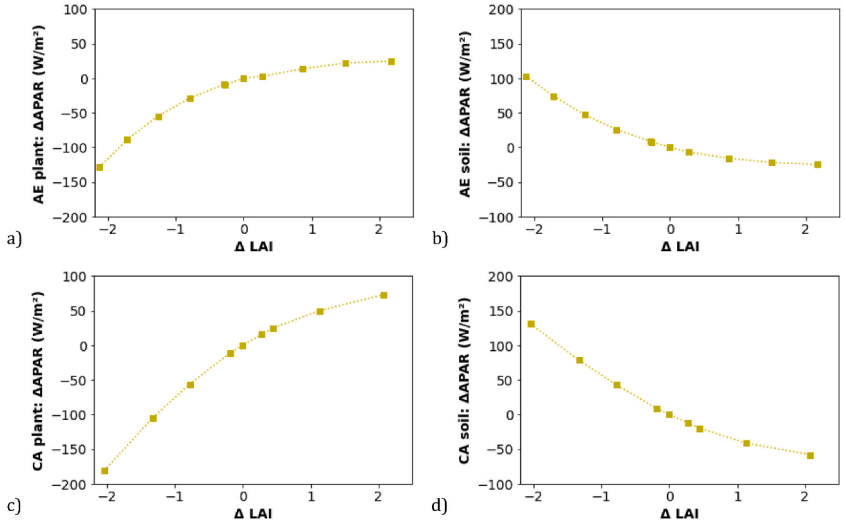

Fig. 16. $\Delta APAR_{plant}$ (a,c) and $\Delta APAR_{soil}$ (b,d) variation of AE and CA fields as a function of variation ΔLAI around the actual case (ΔAPAR = 0, ΔLAI = 0), at 11:00, July 11, 2019.

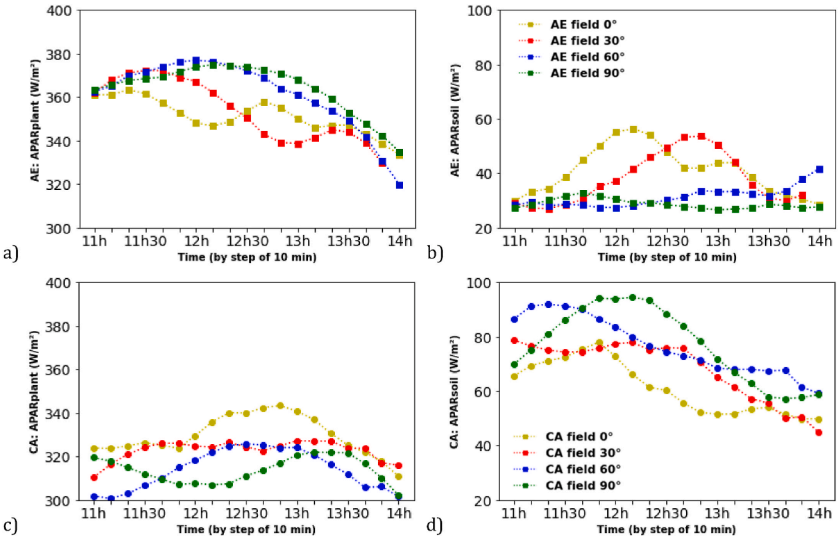

Fig. 17. $APAR_{plant}(t)$ (a,c) and $APAR_{soil}(t)$ (b,d) of AE (a,b) and CA (c,d) fields for 4 row orientations.

Table 5
MTD_{plant} and MTD_{soil} for four row rotations.

Rotation	0°	30°	60°	90°
MTD_{plant} (W/m²)	21.5	30.7	47.4	50.2
MTD_{soil} (W/m²)	−20.1	−31.4	−45.4	−48.2

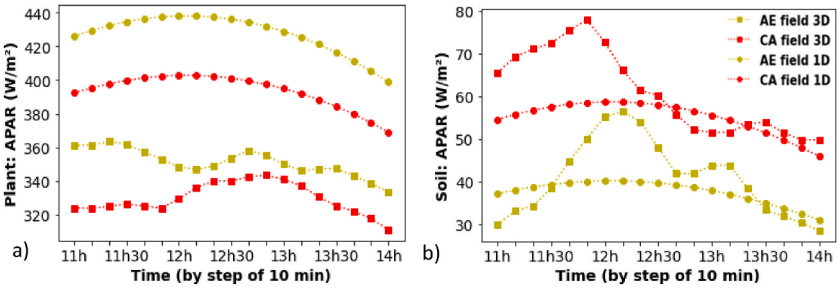

Fig. 18. APAR(t) of plants (a) and soil (b) of AE and CA fields simulated as 1D and 3D models.

CA fields simulated as 3D (i.e., actual field) and 1D models on July 11th, 2019. Time variations of $APAR_{soil}(t)$ and $APAR_{plant}(t)$ are smooth with the 1D models conversely to the 3D models, in particular around 12:30, due to the presence of rows. As expected, 1D models cannot simulate this influence of the 3D architecture of vegetation. Differences are more detailed below.

- $APAR_{soil}(t)$. Over 11am-2pm, the 1D and 3D models give greatly different time variations of $APAR_{soil}(t)$, small mean differences (i.e., 3.3 W/m² for the AE field and 6.0 W/m² for the CA field), and similar differences between the CA and AE fields (*i.e.*, $MTD^{*}_{soil} = -20.1$ W/m² for the 3D models and $MTD^{1D}_{soil} = -17.5$ W/m² for the 1D models).
- $APAR_{plant}(t)$. The 1D and 3D models give greatly different time variations and mean values of $APAR_{plant}(t)$. The mean differences are 76.1 W/m² for the AE field and 63.8 W/m² for the CA field. Also, the 1D and 3D models lead to different differences between the CA and AE fields: $MTD^{1D}_{plant} = 33.8$ W/m² whereas $MTD^{*}_{plant} = 21.5$ W/m². These results are consistent with differences in forest APAR simulated with 1D and 3D models (Regaieg et al., 2021). Conclusions for the maize canopy are similar: the differences in APAR simulated by 1D and 3D models are due to the 3D architecture of the maize fields, and in particular to their row geometry.

6. Conclusion and perspectives

A theoretical 3D physical modeling study with DART on two realistic adjacent maize fields with UAV, satellite and in situ data was achieved. We investigated differences in $APAR_{soil}$ and $APAR_{plant}$ between the maize fields at same stage of development managed in conventional agriculture (CA) and with agroecological practices (AE). We also studied the influence of the field geometry (i.e., inter row and inter plant distances), the plant shape, and the soil and plant optical properties. The theoretical influence of row orientation was also studied.

First, a 3D DART model statistically representative of each field has been created and validated. The methodologies used vegetation indices and spectral reflectance from UAV and Sentinel-2 (S2) images. The creation of the 3D field models, also called DART model calibration, consisted in determining the soil and plant optical properties (OP) and a scale factor for sizing the 3D plant models in order to set the correct LAI. Two calibration methods have been assessed and compared:

- The LAI is fixed, equal to the median SNAP-derived LAI for each field. The pair (OP_{soil}, OP_{plant}) that minimizes differences with S2 reflectance and vegetation indices is selected among all in-situ measured OP_{plant} and OP_{soil}.
- The LAI and (OP_{soil}, OP_{plant}) are adjusted. The pair (OP_{soil}, OP_{plant}) that minimizes differences with reflectance and vegetation indices of UAV at 11 cm or S2 at 10 m resolution is selected among all in-situ measured OP_{plant} and OP_{soil}.

We selected the method based on LAI adjustment using UAV data because the method with fixed LAI from SNAP and OP adjustment did not satisfy the validation criteria. The method of LAI adjustment satisfied the validation criteria with comparison on vegetation indices and reflectance for UAV and S2 with DART. However, the method using UAV data was selected because its fined spatial resolution allowed a statistical comparison of the distribution of reflectance whereas S2 resolution only allowed comparison with a single median value. In addition, a comparison with close reflectance of pure vegetation and soil pixel in DART and UAV images was carried out.

Therefore, two models of the AE and CA fields were created using the method of LAI adjustment combined with UAV data acquired on July 11, 2019. DART simulations using these 3D field models showed differences in APAR between the two fields whereas they have very close LAI. The mean time difference (MTD) in $APAR_{plant}$ and $APAR_{soil}$ over 11 a.m. - 2 p.m. between the CA and AE fields was used to quantify differences between the two fields: $MTD^{*}_{plant} = \text{Mean}\left(APAR^{AE}_{plant}(t) - APAR^{CA}_{plant}(t)\right)$ and $MTD^{*}_{soil} = \text{Mean}\left(APAR^{AE}_{soil}(t) - APAR^{CA}_{soil}(t)\right)$ (*refers to the actual case) We obtained $MTD^{*}_{soil} = -20.1\ W/m^2$ and $MTD^{*}_{plant} = 21.5\ W/m^2$. Then, we investigated these differences by considering separately the main parameters likely to be influential: field geometry (i.e., inter row and plant distances), plant shape of each field (*i.e.*, 3D plant model with its leaf area and geometry), OP_{plant} and OP_{soil}, and LAI.

The share of each parameter in the $APAR_{soil}$ and $APAR_{plant}$ differences between the AE and CA fields has been quantified by replacing one by one each parameter of a field in the other field while keeping the other parameters. We systematically computed the resulting differences between the realistic and modified fields (*i.e.*, $MTD^{AEM\text{-}AE*}_{plant}$, $MTD^{AEM\text{-}AE*}_{soil}$, $MTD^{CAM\text{-}CA*}_{plant}$, $MTD^{CAM\text{-}CA*}_{soil}$), with AE^{M} and CA^{M} being the notations of the modified fields. The share of each parameter is given here as the percentage of the corresponding absolute differences $\left|MTD^{*}_{plant}\right|$ and $\left|MTD^{*}_{soil}\right|$ for the AE (Table 6) and CA (Table 7) fields. The negative value of $MTD^{AEM\text{-}AE*}_{plant} / \left|MTD^{*}_{plant}\right|$ (*i.e.*, −7.5%) in Table 6 indicates that the AE geometry favours $APAR_{plant}$. Symmetrically, and in a more marked way, the positive value of $MTD^{CAM\text{-}CA*}_{plant} / \left|MTD^{*}_{plant}\right|$ (*i.e.*, 26.3%) in Table 7 indicates that the CA geometry disadvantages $APAR_{plant}$. Excepted LAI which usually increases $APAR_{plant}$ and directly impacts the effect of the other parameters, OP_{soil} has the largest share both for $APAR_{soil}$ and $APAR_{plant}$. For example, the negative value of $MTD^{AEM\text{-}AE*}_{plant} / \left|MTD^{*}_{plant}\right|$ (i.e., −44.2%) associated to the use of OP^{CA}_{soil} in the AE field is explained by the fact that the AE soil with its residues absorbs less and scatters more radiation to the plants than the CA soil. It is interesting to note that the role of the AE geometry added to that of the AE plant model are far from negligible maximizing both $APAR_{plant}$. The sensitivity of LAI to APAR was also studied. It appeared to be two times higher for the CA field than for the AE field near the real field conditions (e.g., LAI ≈ 3).

The influence of the maize row orientation on $APAR_{soil}$, $APAR_{plant}$, MTD_{plant} and MTD_{soil} was studied. It showed that in the well-structured CA field, at noon, $APAR_{soil}$ is maximal with North-South rows (i.e., solar direction parallel to the rows at noon) and $APAR_{plant}$ is maximal with East-West rows (i.e., solar direction perpendicular to the rows at noon). It is nearly the opposite for the AE field. This is mostly explained by the fact that rows in the AE field are much less marked. Indeed, the ratio “inter-row / inter-plant dis-

Table 6
Share (%) of MTD on $APAR_{plant}$ and $APAR_{soil}$ of each CA parameter: ratio of the difference $MTD^{AEM-AE*}_{plant}$ or $MTD^{AEM-AE*}_{soil}$ between the real and modified AE fields by the absolute difference $\left|MTD^{*}_{plant}\right|$ or $\left|MTD^{*}_{soil}\right|$ between the CA and AE real fields.

Swapped parameter in AE field model	CA geometry	OP^{CA}_{soil}	OP^{CA}_{plant}	CA plant model	$LAI_{CA} = 3.2$
$MTD^{AEM\text{-}AE*}_{plant} / \left|MTD^{*}_{plant}\right|$	−7.5 %	−44.2 %	−15.4 %	−19.4 %	−40.8 %
$MTD^{AEM\text{-}AE*}_{soil} / \left|MTD^{*}_{soil}\right|$	2.8 %	45.1 %	0,9 %	18.1 %	36.7 %

Table 7
Share (%) of MTD on $APAR_{plant}$ and $APAR_{soil}$ of each CA parameter: ratio of the difference $MTD^{CAM-CA*}_{plant}$ or $MTD^{CAM-CA*}_{soil}$ between the real and modified CA fields by the absolute difference $\left|MTD^{*}_{plant}\right|$ or $\left|MTD^{*}_{soil}\right|$ between the CA and AE real fields.

Swapped parameter in CA field model	AE geometry	OP^{AE}_{soil}	OP^{AE}_{plant}	AE plant model	$LAI_{AE} = 3.5$
$MTD^{CAM\text{-}CA*}_{plant} / \left|MTD^{*}_{plant}\right|$	26.3 %	48.7 %	13.9 %	14.4 %	52.2 %
$MTD^{CAM\text{-}CA*}_{soil} / \left|MTD^{*}_{soil}\right|$	−23.7 %	−53.9 %	−1.8 %	−17.2 %	−42.3 %

tances" is 6.4 for the CA field and 1.6 for the AE field. he differences between the AE and CA fields (i.e., the MTD^{*}_{soil} MTD and MTD^{*}_{plant}) are minimal with the actual "East-West" row orientation and maximal with the theoretical 90° rotation to the North-South orientation. It is interesting to note that taking into account of the row orientation in vegetation studies is facilitated by cartographic products with row orientation increasingly derived from remote sensing data (https://eolab.cnes.fr/projets/orientation-des-cultures-agricoles).

The way the vegetation canopy is modelled greatly influences simulations of APAR and remote sensing observations. It was illustrated by comparing simulations of APAR for vegetation represented by 3D and 1D models. It showed that 3D and 1D models lead to very different hourly variations of APAR. These variations are very smooth with 1D models due to their azimuthal symmetry unlike the 3D model due to dissymmetry induced by rows. It results a non-smooth hourly variation of APAR that 1D models cannot reproduce. In addition, compared to the 3D model, the 1D model with the same LAI greatly overestimates $APAR_{plant}$ and underestimates $APAR_{soil}$. This is consistent with the 3D heterogeneity of canopies where the clumping of vegetation tends to increase the transmittance of vegetation. Here, $APAR_{plant}$ is overestimated by 76.1 W/m^2 for the AE field and 63.8 W/m^2 for the CA field (≈20% relative increase). These findings raise questions about the suitability of using 1D models to study APAR at fine scales.

Studies on maize have shown a direct link between reduced radiation in PAR and reduced productivity (Yang et al., 2022). By decreasing PAR radiation by 15% depending on the maize variety, the number of grains per row can decrease by 7.2%, bald tip lengths can be 1.4 times higher and the grain abortion rates can increase by 5.3%. In our study, we found a decrease in APAR of about 6.5% in the realistic case between AE and CA, and this difference can reach 16.2% with a 90° field rotation from the realistic case, which frequently occurs in the study region. It can therefore be argued that the modulation of PAR radiation caused by AE agricultural practice can have a direct consequence on maize yield.

Additional parameters could be considered in order to improve the accuracy of the work. For example, the vertical range of $APAR_{plant}$ in relation with the vertical range of OP_{plant}. Depending on the season, the vertical profile of OP_{plant} can be very broad, with brown leaves at the base of the maize plant and green leaves at the top. This is possible with 3D models such as DART.

Another major work is to simulate the RB in the thermal domain with DART, possibly using 3D models of fields calibrated with UAV data. Indeed, the RB in the thermal infrared domain greatly influences plant physiology. This is of particular importance in the context of next thermal infrared space missions (TRISHNA, LSTM, Lagouarde et al., 2019). UAV thermal infrared data can provide a high-resolution distribution of brightness temperature in the CA and AE fields. The creation of 3D models directly with high resolution stereo photogrammetry or LiDAR techniques are also interesting paths to explore, in particular to get the spatial distribution of LAI in each field.

Ethical statement

I declare that all ethical practices have been followed in relation to the development, writing, and publication of the article.

Declaration of competing interest

The authors declare that they have no known competing financial interests or personal relationships that could have appeared to influence the work reported in this paper.

Data availability

Data will be made available on request.

Acknowledgments

The authors thank the Research Council of the Institute of Technology of Toulouse III University and the french Occitanie Region that funded the PhD of P. Boitard (grant n°20007276-000992), the TOSCA program "TRISHNA space mission (french PI: J.L. Roujean) " of CNES national space center, CNES EO-Lab for data on crop field orientation (https://eolab.cnes.fr/), GEODE (https://geode.univ-tlse2.fr/), especially H. Barcet for UAV data, and DART team members, especially E. Chavanon and J. Guilleux for their precious help on computer codes.

References

Albert, M., Bergez, J.E., Couture, S., Faivre, R., Willaume, M., 2021. Decision-making process factors explain some of the heterogeneity of irrigation practices among maize farmers in southwestern France. Water (Switzerland) 13 (24). https://doi.org/10.3390/w13243504.

Altieri, M.A., Nicholls, C.I., Henao, A., Lana, M.A., 2015. Agroecology and the design of climate change-resilient farming systems. Agron. Sustain. Dev. 35 (Issue 3). https://doi.org/10.1007/s13593-015-0285-2.

BAGAGES, 2021. https://www.eau-grandsudouest.fr/agenda/restitution-projet-bag-ages.

Bajocco, S., Ginaldi, F., Savian, F., Morelli, D., Scaglione, M., Fanchini, D., Raparelli, E., Bregaglio, S.U.M., 2022. On the use of NDVI to estimate LAI in field crops: implementing a conversion equation library. Rem. Sens. 14, 3554. https://doi.org/10.3390/rs14153554.

Battude, M., al Bitar, A., Brut, A., Tallec, T., Huc, M., Cros, J., Weber, J.J., Lhuissier, L., Simonneaux, V., Demarez, V., 2017. Modeling water needs and total irrigation depths of maize crop in the south west of France using high spatial and temporal resolution satellite imagery. Agric. Water Manag. 189. https://doi.org/10.1016/j.agwat.2017.04.018.

Brede, B., Verrelst, J., Gastellu-Etchegorry, J.P., Clevers, J.G.P.W., Goudzwaard, L., den Ouden, J., Verbesselt, J., Herold, M., 2020. Assessment of workflow feature selection on forest LAI prediction with sentinel-2A MSI, landsat 7 ETM+ and Landsat 8 OLI. Rem. Sens. 12 (6). https://doi.org/10.3390/rs12060915.

Brye, K.R., Norman, J.M., Bundy, L.G., Gower, S.T., 2000. Water-budget evaluation of prairie and maize ecosystems. Soil Sci. Soc. Am. J. 64 (2). https://doi.org/10.2136/sssaj2000.642715x.

Colas-Belcour, et al., 2015. https://agriculture.gouv.fr/sites/minagri/files/cgaaer_14061_2015_rapport.pdf.

Cueff, S., Alletto, L., Dumény, V., Benoit, P., Pot, V., 2021. Adsorption and degradation of the herbicide nicosulfuron in a stagnic Luvisol and Vermic Umbrisol cultivated under conventional or conservation agriculture. Environ. Sci. Pollut. Control Ser. 28 (13). https://doi.org/10.1007/s11356-020-11772-2.
Cueff, S., Alletto, L., Bourdat-Deschamps, M., Benoit, P., Pot, V., 2020. Water and pesticide transfers in undisturbed soil columns sampled from a Stagnic Luvisol and a Vermic Umbrisol both cultivated under conventional and conservation agriculture. Geoderma 377. https://doi.org/10.1016/j.geoderma.2020.114590.
De Benedetto, D., Montemurro, F., Diacono, M., 2017. Impacts of agro-ecological practices on soil losses and cash crop yield. Agriculture (Switzerland) 7 (12). https://doi.org/10.3390/agriculture7120103.
DRAAF, 2018. https://draaf.occitanie.agriculture.gouv.fr/l-irrigation-contribue-a-18-de-la-valeur-de-la-production-agricole-analyses-a5054.html.
Dupiau, A., Jacquemoud, S., Briottet, X., Fabre, S., Viallefont-Robinet, F., Philpot, W., di Biagio, C., Hébert, M., Formenti, P., 2022. MARMIT-2: an improved version of the MARMIT model to predict soil reflectance as a function of surface water content in the solar domain. Rem. Sens. Environ. 272. https://doi.org/10.1016/j.rse.2022.112951.
Duthoit, S., Demarez, V., Gastellu-Etchegorry, J.P., Martin, E., Roujean, J.L., 2008. Assessing the effects of the clumping phenomenon on BRDF of a maize crop based on 3D numerical scenes using DART model. Agric. For. Meteorol. 148 (8–9). https://doi.org/10.1016/j.agrformet.2008.03.011.
Fan, X., Vrieling, A., Muller, B., Nelson, A., 2020. Winter cover crops in Dutch maize fields: variability in quality and its drivers assessed from multi-temporal Sentinel-2 imagery. Int. J. Appl. Earth Obs. Geoinf. 91. https://doi.org/10.1016/j.jag.2020.102139.
Feret, J.B., François, C., Asner, G.P., Gitelson, A.A., Martin, R.E., Bidel, L.P.R., Ustin, S.L., le Maire, G., Jacquemoud, S., 2008. PROSPECT-4 and 5: advances in the leaf optical properties model separating photosynthetic pigments. Rem. Sens. Environ. 112 (6). https://doi.org/10.1016/j.rse.2008.02.012.
Ferreira, T. de A., Ferreira, S.C., Barbosa, J.A., Volpato, C.E.S., Ferreira, R.C., da Silva, M.J., Barbosa, L.M., 2018. Energy balance of irrigated maize silage. Ciência Rural. 48 (5). https://doi.org/10.1590/0103-8478cr20170625.
Gastellu-Etchegorry, J.P., Demarez, V., Pinel, V., Zagolski, F., 1996. Modeling radiative transfer in heterogeneous 3-D vegetation canopies. Rem. Sens. Environ. 58 (2). https://doi.org/10.1016/0034-4257(95)00253-7.
Gastellu-Etchegorry, J.P., Lauret, N., Yin, T., Landier, L., Kallel, A., Malenovský, Z., al Bitar, A., Aval, J., Benhmida, S., Qi, J., Medjdoub, G., Guilleux, J., Chavanon, E., Cook, B., Morton, D., Chrysoulakis, N., Mitraka, Z., 2017. DART: recent advances in remote sensing data modeling with atmosphere, polarization, and chlorophyll fluorescence. IEEE J. Sel. Top. Appl. Earth Obs. Rem. Sens. 10 (6). https://doi.org/10.1109/JSTARS.2017.2685528.
Genet, A.T., Tewabe, D., Abebe, A., Enyew, A., Worku, M., 2022. Effect of irrigation regime on yield and water productivity of maize (zea mays) in the lake tana basin, north west Ethiopia. Turkish J. Agric. - Food Sci. Technol. 10 (2). https://doi.org/10.24925/turjaf.v10i2.100-105.3982.
Gingrich, S., Marco, I., Aguilera, E., Padró, R., Cattaneo, C., Cunfer, G., Guzmán, G.I., MacFadyen, J., Watson, A., 2018. Agroecosystem energy transitions in the old and new worlds: trajectories and determinants at the regional scale. Reg. Environ. Change 18 (4). https://doi.org/10.1007/s10113-017-1261-y.
Hellin, J., Erenstein, O., Beuchelt, T., Camacho, C., Flores, D., 2013. Maize stover use and sustainable crop production in mixed crop-livestock systems in Mexico. Field Crops Res. 153. https://doi.org/10.1016/j.fcr.2013.05.014.
Hernández-Clemente, R., Navarro-Cerrillo, R.M., Zarco-Tejada, P.J., 2012. Carotenoid content estimation in a heterogeneous conifer forest using narrow-band indices and PROSPECT + DART simulations. Rem. Sens. Environ. 127. https://doi.org/10.1016/j.rse.2012.09.014.
IPCC, 2022. IPCC climate change 2022 impacts, adapataion and vulnerability summary for policymakers. In: Implementing a US Carbon Tax: Challenges and Debates.
IUSS Working Group WRB, 2007. World Reference Base For Soil Resources 2006, first update. A framework for international classification, correlation and communication. FAO, Food and Agriculture Organization of the United Nations, Rome.
Jankowski, K.J., Dubis, B., Sokólski, M.M., Załuski, D., Bórawski, P., Szempliński, W., 2020. Productivity and energy balance of maize and sorghum grown for biogas in a large-area farm in Poland: an 11-year field experiment. Ind. Crop. Prod. 148. https://doi.org/10.1016/j.indcrop.2020.112326.
Jiang, Jingyi, Weiss, Marie, Liu, Shouyang, 2022. Frédéric Baret, Effective GAI is best estimated from reflectance observations as compared to GAI and LAI: demonstration for wheat and maize crops based on 3D radiative transfer simulations. Field Crops Res. 283. https://doi.org/10.1016/j.fcr.2022.108538. 108538, ISSN 0378-4290.
Kganyago, M., Mhangara, P., Alexandridis, T., Laneve, G., Ovakoglou, G., Mashiyi, N., 2020. Validation of sentinel-2 leaf area index (LAI) product derived from SNAP toolbox and its comparison with global LAI products in an African semi-arid agricultural landscape. Rem. Sens. Lett. 11 (10). https://doi.org/10.1080/2150704X.2020.1767823.
Lagouarde, J.-P., Bhattacharya, B.K., Crébassol, P., Gamet, P., Adlakha, D., Murthy, C.S., Singh, S.K., Mishra, M., Nigam, R., Raju, P.V., Babu, S.S., Shukla, M.V., Pandya, M.R., Boulet, G., Briottet, X., Dadou, I., Dedieu, G., Gouhier, M., Hagolle, O., Irvine, M., Jacob, F., Kumar, K.K., Laignel, B., Maisongrande, P., Mallick, K., Olioso, A., Ottlé, C., Roujean, J.-L., Sobrino, J., Ramakrishnan, R., Sekhar, M., Sarkar, S.S., 2019. INDO-French high-resolution thermal infrared space mission for earth natural resources assessment and monitoring – concept and definition of TRISHNA. Int. Arch. Photogram. Rem. Sens. Spatial Inf. Sci. 403–407. https://doi.org/10.5194/isprs-archives-XLII-3-W6-403-2019. XLII-3/W6.
Laliberte, A.S., Goforth, M.A., Steele, C.M., Rango, A., 2011. Multispectral remote sensing from unmanned aircraft: image processing workflows and applications for rangeland environments. Rem. Sens. 3 (11). https://doi.org/10.3390/rs3112529.
Malenovský, Z., Regaieg, O., Yin, T., Lauret, N., Guilleux, J., Chavanon, E., Duran, N., Janoutová, R., Delavois, A., Meynier, J., Medjdoub, G., Yang, P., van der Tol, C., Morton, D., Cook, B.D., Gastellu-Etchegorry, J.P., 2021. Discrete anisotropic radiative transfer modelling of solar-induced chlorophyll fluorescence: structural impacts in geometrically explicit vegetation canopies. Rem. Sens. Environ. 263. https://doi.org/10.1016/j.rse.2021.112564.
Marais-Sicre, Claire, Queguiner, Solen, Bustillo, Vincent, Lesage, Luka, Barcet, Hugues, Pellé, Nathalie, Breil, Nicolas, Benoit, Coudert., 2023. Sun/shade separation in optical and thermal UAV images for assessing the impact of agricultural practices. Remote Sensing (MDPI). . under review.
Meyers, T.P., Hollinger, S.E., 2004. An assessment of storage terms in the surface energy balance of maize and soybean. Agric. For. Meteorol. 125 (1–2). https://doi.org/10.1016/j.agrformet.2004.03.001.
Naylor, R.L., 1996. Energy and resource constraints on intensive agricultural production. Annu. Rev. Energy Environ. 21 (1). https://doi.org/10.1146/annurev.energy.21.1.99.
Nebiker, S., Lack, N., Abächerli, M., Läderach, S., 2016. Light-weight multispectral uav sensors and their capabilities for predicting grain yield and detecting plant diseases. In: International Archives of the Photogrammetry, Remote Sensing and Spatial Information Sciences. ISPRS Archives. https://doi.org/10.5194/isprsarchives-XLI-B1-963-20162016-January.
Ofgeha, G.Y., Abshire, M.W., 2021. Spatio-temporal variability and trends in rainfall and temperature in anger watershed, southwestern Ethiopia. J. Appl. Geospatial Informat. 5 (1). https://doi.org/10.30871/jagi.v5i1.2825.
Raeva, P.L., Šedina, J., Dlesk, A., 2019. Monitoring of crop fields using multispectral and thermal imagery from UAV. Eur. J. Rem. Sens. 52 (Suppl. 1). https://doi.org/10.1080/22797254.2018.1527661.
Reddy, K.S., Kumar, M., Maruthi, V., Lakshminarayana, P., Vijayalakshmi, Umesha, B., Reddy, Y.V.K., 2016. Climate change impacts on crop water balance of maize (Zea mays L.) in lower Krishna River Basin of South India. Curr. Sci. 111 (3). https://doi.org/10.18520/cs/v111/i3/565-570.
Regaieg, O., Yin, T., Malenovský, Z., Cook, B.D., Morton, D.C., Gastellu-Etchegorry, J.P., 2021. Assessing impacts of canopy 3D structure on chlorophyll fluorescence radiance and radiative budget of deciduous forest stands using DART. Rem. Sens. Environ. 265. https://doi.org/10.1016/j.rse.2021.112673.
Ren, T., Liu, Z., Zhang, L., Liu, D., Xi, X., Kang, Y., Zhao, Y., Zhang, C., Li, S., Zhang, X., 2020. Early identification of seed maize and common maize production fields using sentinel-2 images. Rem. Sens. 12 (13). https://doi.org/10.3390/rs12132140.
Sagan, Vasit, Maimaitijiang, Maitiniyazi, Sidike, Paheding, Eblimit, Kevin, Peterson, Kyle, Hartling, Sean, Esposito, Flavio, Khanal, Kapil, Newcomb, Maria, Pauli, William, Ward, Richard, Fritschi, Felix, Shakoor, Nadia, Mockler, Todd, 2019. UAV-based high resolution thermal imaging for vegetation monitoring, and plant phenotyping using ICI 8640 P, FLIR vue pro R 640, and thermoMap cameras. Rem. Sens. 11, 330. https://doi.org/10.3390/rs11030330.
Schoonhoven, Y., Runhaar, H., 2018. Conditions for the adoption of agro-ecological farming practices: a holistic framework illustrated with the case of almond farming in Andalusia. Int. J. Agric. Sustain. 16 (6). https://doi.org/10.1080/14735903.2018.1537664.
Sepulcre-Cantó, G., Zarco-Tejada, P.J., Sobrino, J.A., Berni, J.A.J., Jiménez-Muñoz, J.C., Gastellu-Etchegorry, J.P., 2009. Discriminating irrigated and rainfed olive orchards with thermal ASTER imagery and DART 3D simulation. Agric. For. Meteorol. 149 (6–7). https://doi.org/10.1016/j.agrformet.2008.12.001.
Smith, A.M., Bourgeois, G., Teillet, P.M., Freemantle, J., Nadeau, C., 2008. A comparison of NDVI and MTVI2 for estimating LAI using CHRIS imagery: a case study in wheat. Can. J. Rem. Sens. 34 (6). https://doi.org/10.5589/m08-071.

Sobrino, J.A., Mattar, C., Gastellu-Etchegorry, J.P., Jiménez-Muñoz, J.C., Grau, E., 2011. Evaluation of the DART 3D model in the thermal domain using satellite/airborne imagery and ground-based measurements. Int. J. Rem. Sens. 32 (22). https://doi.org/10.1080/01431161.2010.524672.

Soltner, 2018. Agroécologie : Guide de la nouvelle agriculture. Collection Sciences et Techniques Agricoles. ISBN N°2-907710-28-1.

Van der Velde, M., Wriedt, G., Bouraoui, F., 2010. Estimating irrigation use and effects on maize yield during the 2003 heatwave in France. Agric. Ecosyst. Environ. 135 (1–2). https://doi.org/10.1016/j.agee.2009.08.017.

Walker, S., Ogindo, H.O., 2003. The water budget of rainfed maize and bean intercrop. Physics and Chemistry of the Earth 28 (20–27). https://doi.org/10.1016/j.pce.2003.08.018.

Wang, Y., Kallel, A., Yang, X., Regaieg, O., Lauret, N., Guilleux, J., Chavanon, E., Gastellu-Etchegorry, J.P., 2022. DART-Lux: an unbiased and rapid Monte Carlo radiative transfer method for simulating remote sensing images. Rem. Sens. Environ. 274. https://doi.org/10.1016/j.rse.2022.112973.

Wei, S., Yin, T., Dissegna, M.A., Whittle, A.J., Ow, G.L.F., Yusof, M.L.M., Lauret, N., Gastellu-Etchegorry, J.P., 2020. An assessment study of three indirect methods for estimating leaf area density and leaf area index of individual trees. Agric. For. Meteorol. 292–293. https://doi.org/10.1016/j.agrformet.2020.108101.

Weiss, M., Baret, F., Jay, S., 2020. S2 Tool Box Level 2 Products LAI, FAPAR, fCOVER. [ResearchReport] EMMAH-CAPTE. INRAe Avignon. Hal-03584016.

Wen, W., Guo, X., Li, B., Wang, C., Wang, Y., Yu, Z., Wu, S., Fan, J., Gu, S., Lu, X., 2019. Estimating canopy gap fraction and diffuse light interception in 3D maize canopy using hierarchical hemispheres. Agric. For. Meteorol. 276–277. https://doi.org/10.1016/j.agrformet.2019.05.025.

Wen, W., Wang, Y., Wu, S., Liu, K., Gu, S., Guo, X., 2021. 3D phytomer-based geometric modelling method for plants-the case of maize. AoB PLANTS 13 (5). https://doi.org/10.1093/aobpla/plab055.

Widlowski, J.L., Mio, C., Disney, M., Adams, J., Andredakis, I., Atzberger, C., Brennan, J., Busetto, L., Chelle, M., Ceccherini, G., Colombo, R., Côté, J.F., Eenmäe, A., Essery, R., Gastellu-Etchegorry, J.P., Gobron, N., Grau, E., Haverd, V., Homolová, L., et al., 2015. The fourth phase of the radiative transfer model intercomparison (RAMI) exercise: actual canopy scenarios and conformity testing. Rem. Sens. Environ. 169. https://doi.org/10.1016/j.rse.2015.08.016.

Yang, P., Prikaziuk, E., Verhoef, W., van der Tol, C., 2021. Scope 2.0: a model to simulate vegetated land surface fluxes and satellite signals. Geosci. Model Dev. (GMD) 14 (7). https://doi.org/10.5194/gmd-14-4697-2021.

Yang, Y., Liu, G., Guo, X., Liu, W., Xue, J., Ming, B., Xie, R., Wang, K., Li, S., Hou, P., 2022. Effect mechanism of solar radiation on maize yield formation. Agriculture (Switzerland) 12 (12). https://doi.org/10.3390/agriculture12122170.

Zhao, M.B., 2015. Moment Distribution Method to Compute the Moment of Continuous Beam Using WPS. https://doi.org/10.2991/iccet-15.2015.15.